A Satellite-Based Climatology of Central and Southeastern U.S. Mesoscale Convective Systems

SHAWN M. CHEEKS AND STEPHAN FUEGLISTALER

Princeton University, Princeton, New Jersey

STEPHEN T. GARNER

NOAA/GFDL, Princeton, New Jersey

(Manuscript received 28 January 2020, in final form 13 April 2020)

ABSTRACT

A satellite-based climatology is presented of 9607 mesoscale convective systems (MCSs) that occurred over the central and southeastern United States from 1996 to 2017. This climatology is constructed with a fully automated algorithm based on their cold cloud shields, as observed from infrared images taken by GOES-East satellites. The geographical, seasonal, and diurnal patterns of MCS frequency are evaluated, as are the frequency distributions and seasonal variability of duration and maximum size. MCS duration and maximum size are found to be strongly correlated, with coefficients greater than 0.7. Although previous literature has subclassified MCSs based on size and duration, we find no obvious threshold that cleanly categorizes MCSs. The Plains and Deep South are identified as two regional modes of maximum MCS frequency, accounting for 21% and 18% of MCSs, respectively, and these are found to differ in the direction and speed of the MCSs (means of 16 and 13 $m\,s^{-1}$), their distributions of duration and size (means of 12.2 h, 176 000 km^2 and 9.6 h, 108 000 km^2), their initial growth rates (means of 7.6 and 6.1 $km^2\,s^{-1}$), and many aspects of the seasonal cycle. The lifetime patterns of MCS movement and growth are evaluated for the full domain and for the two regional modes. The growth patterns and strong correlation between size and duration allow for a parabolic function to represent the MCS life cycle quite well in summary statistics. We show that this satellite-based climatology supports previous studies identifying favorable environments for mesoscale convective systems.

1. Introduction

Mesoscale convective systems (MCSs) are thunderstorm complexes that organize on scales of hundreds of kilometers and several hours. As a result, they are responsible for a significant amount of severe weather and over half of global precipitation (Cotton et al. 1995). Although MCSs occur in many locations around the globe, they are focused on locations with baroclinicity, vertical wind shear, CAPE, and frequent low-level jets (LLJ) of warm, moist air (Laing and Fritsch 1997, 2000). The focus of this paper is the central and southeastern United States, one of the most active regions for MCS occurrence.

MCSs typically begin with a group of convective cells that organize due to their proximity or due to shared initial forcing, such as by a front. As new cells form, the older cells weaken and evolve into a broad, contiguous region of stratiform precipitation (e.g., Houze 1982). The coexistence of convective and stratiform components is a hallmark of mature MCSs (Houze 1997). The end of an MCS life cycle is marked by the weakening of its convection and ultimately the stanching of the stratiform component that is sustained by the convection. The relationship between these two components are the foundation for radar-based MCS classification schemes (Parker and Johnson 2000); however, to be consistent with previous satellite-based literature (e.g., Maddox 1980; Augustine and Howard 1988; Anderson and Arritt 1998, 2001; Jirak et al. 2003), this paper utilizes a single-threshold satellite-based approach that cannot distinguish between convective and stratiform clouds.

The literature on the processes controlling MCS initiation and maintenance is among the most extensive in

Supplemental information related to this paper is available at the Journals Online website: https://doi.org/10.1175/MWR-D-20-0027.s1.

Corresponding author: Shawn M. Cheeks, scheeks@princeton.edu

DOI: 10.1175/MWR-D-20-0027.1

dynamical meteorology. To provide context for our findings, we include here a summary of the main ideas. The convective component requires a continuous inflow of moisture, such as from a low-level jet (LLJ, Maddox 1983), while the stratiform component is comprised of remnant ice particles from convection that are kept aloft by a broader, mesoscale updraft (Leary and Houze 1979; Yuter and Houze 1995). These sustaining conditions are heavily influenced by synoptic patterns, especially the North Atlantic subtropical high (NASH). The NASH's seasonal migration and interannual variability modulate the precipitation patterns of the central and southeastern United States (Li et al. 2012). MCSs regularly occur ahead of troughs (Maddox 1983), and these troughs have been shown to enhance the Great Plains LLJ during MCS activity (Trier and Parsons 1993).

Convective initiation over the Great Plains is most frequent overnight, as recently confirmed by the Plains Elevated Convection At Night (PECAN; Geerts et al. 2017) campaign (e.g., Reif and Bluestein 2017; Weckwerth et al. 2019). This accounts for the nighttime climatological precipitation maximum in the region (e.g., Riley et al. 1987; Higgins et al. 1997; Weckwerth and Romatschke 2019). The convection has different triggers, including the LLJ terminus, LLJ overrunning (of a front), influences from a preexisting MCS, bores, and gravity waves (Weckwerth et al. 2019). The LLJ is a diurnal phenomenon that arises from a combination of nightly decoupling of the boundary layer from the surface (Blackadar 1957) and horizontal temperature differences due to elevation changes across the Great Plains (Holton 1967). The temperature differences are part of the mountain–plains solenoid (MPS), a diurnal overturning circulation, similar to a land–sea-breeze circulation, that modulates the location and timing of MCS activity across the region (Wolyn and Mckee 1994; Dai et al. 1999; Carbone and Tuttle 2008).

MCSs can generate a mesoscale convective vortex (MCV) through the potential vorticity anomaly generated by the top-heavy profile of diabatic heating (Johnston 1981; Bartels and Maddox 1991; Fritsch et al. 1994). The MCV can then outlive the MCS itself and modify the environment to encourage future MCS development. The outflow boundaries of active MCSs can also cause new convection (Weckwerth et al. 2019). Specifically, bores and density currents are hydraulic jumps that have also been shown to trigger nocturnal convection and contribute to MCS initiation (Geerts et al. 2017; Haghi et al. 2017, 2019; Parsons et al. 2019).

Although MCSs commonly require favorable synoptic environments, they can also initiate with only local forcings, such as a land–sea breeze or MPS, if the environment has high surface temperature and humidity (e.g., Song et al. 2019, hereafter S19). While MCSs occur in the presence of CAPE and vertical wind shear, there is evidence that too much shear limits MCS duration (Yang et al. 2017), and environments with more CAPE and shear favor development of supercells rather than MCSs (Thompson et al. 2012). Extensive details of MCS dynamics can be found in the AMS Centennial Monograph on MCSs (Houze 2018).

Large-scale, methodologically consistent historical records are valued for providing a reliable context for assessing models and theory. With the development of new techniques and improved computing capabilities, more observations have allowed more studies on MCSs in the United States. Despite this, only two studies span longer than a decade with homogeneous datasets: Haberlie and Ashley (2019, hereafter HA19) and Feng et al. (2019, hereafter F19), both of which utilize radar data to characterize MCSs.

MCSs are frequently studied through the lens of geostationary infrared satellite imagery because they produce large cloud shields—contiguous regions of extremely cold cloud-top temperatures—that are easily identifiable and trackable in infrared satellite images. Furthermore, geostationary satellite imagery has extensive spatial and temporal coverage, and the methods for analyzing geostationary satellite data can be applied to any region of the globe. To date, the satellite-based histories of central and southeastern U.S. MCSs are relatively brief (e.g., Maddox 1980; Augustine and Howard 1988; Anderson and Arritt 1998, 2001; Jirak et al. 2003). Composite climatologies have also been constructed from the short surveys (e.g., Bartels et al. 1984; Ashley et al. 2003). For example, Ashley et al. (2003) constructed a 15-yr dataset by compiling results from nine different short-duration studies that examined years from 1978 to 1999. While they took care to minimize differences between the different studies, their composite was limited by the scopes of the component studies, and they were only able to study 15 of the 22 years in their 1978–99 domain.

This paper provides a comprehensive satellite-based climatology of central and southeastern U.S. MCSs for the 22-yr period of 1996–2017. We utilize a fully automated "area-overlap" procedure, adapted from Whitehall et al. (2015), which itself is an implementation of the algorithm presented in Williams and Houze (1987). Our implementation differs from other satellite-based processing techniques (such as Carvalho and Jones 2001; Vila et al. 2008; Hennon et al. 2011; Fiolleau and Roca 2013) in that data are stored in a graph database that intrinsically accounts for system mergers and splits. Similar decade-long satellite-based studies in other parts of the world (e.g., Durkee and Mote 2010; Blamey and Reason 2012) have required human intervention to process mergers and splits. By using a graph database to represent the complex MCS life cycles, we remove a potential source of subjectivity and allow the algorithm to construct the climatology without human intervention beyond the defining parameters. The details of this graph database are described in section 2.

In examining the spatial, seasonal, and diurnal patterns of MCS frequency, duration, and size, we find that there are no obvious thresholds of duration and size that cleanly subcategorize MCSs, as has been commonly done in previous satellite-based studies (e.g., Anderson and Arritt 1998, 2001; Jirak et al. 2003). The Plains (PL) and Deep South (DS) are identified, however, as two regional modes of maximum MCS frequency (Fig. 1). These differ substantially from each other and from the patterns of the overall domain. MCSs in PL become common earlier in the season, move faster, travel farther, obtain a larger maximum size, and have a longer duration. Those in DS, while having duration and size patterns similar to the full domain, typically move slower, travel less distance, and have a shorter-lived active season than the domain as a whole.

The lifetime patterns of MCS movement and growth are considered for the overall domain and the two regional modes. Size and duration are shown to be strongly correlated in all three, and using this strong correlation, a parabolic function is demonstrated to closely represent MCS summary statistics. The life cycle of size for an individual MCS does not always closely follow a parabola, but we show that a parabola is a useful characterization of the average of large collections of MCSs.

We begin in section 2 with descriptions of the data and techniques, including a description of the graph database. Section 3 presents the spatial and temporal patterns of the MCSs, which reveal the preferred locations for MCSs to occur and how the favorable locations change temporally across the domain. In section 4, we evaluate two of the defining characteristics: duration and size. The distributions of duration and maximum size are presented and shown to be strongly correlated, the typical lifetime of MCS growth and decay are described, and the quadratic time behavior of the composite is demonstrated. Finally, in section 5, we discuss possible dynamical implications of the results and suggest future directions of study.

2. Data and methods

a. Data

GOES-East infrared satellite imagery for this study are provided by NOAA's Comprehensive Large Array-Data Stewardship System (CLASS), which is hosted by the

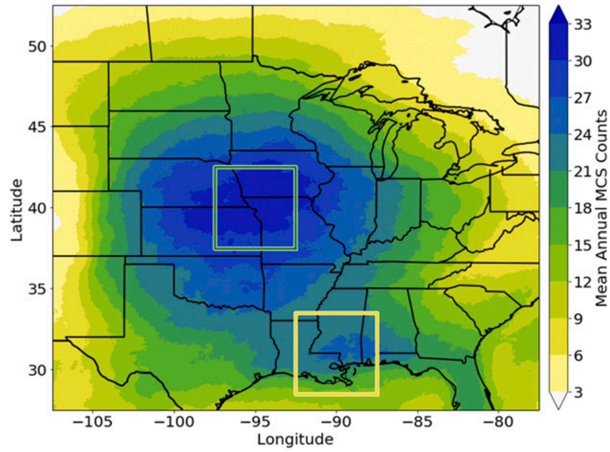

FIG. 1. Map of mean annual frequency of MCS cloud shields passing overhead. Boxes indicate the 5° boundary defining the analysis regions for the Plains (PL, green) and Deep South (DS, yellow) modes.

National Centers for Environmental Information (NCEI). In the 22 years examined, four satellites served as GOES-East: *GOES-8*, *GOES-12*, *GOES-13*, and *GOES-14*. Because this study does not evaluate interannual trends, any instrumental changes across successive satellites are not expected to substantially affect results. All four satellites' infrared images have a nominal 4 km resolution, and all images were regridded to a 0.025° latitude–longitude grid for analysis.

The GOES-East satellite typically produces an infrared image of the continental United States every 15 min. However, there are occasional irregularities in the data from instrument failure, transmission problems, or temporary schedule changes. We address data irregularities by removing images that are incomplete within 20°–55°N and 65°–115°W, which is the full domain for this study. For images that are complete, many have a few pixel-wide lines of erroneous data. To keep these images in the dataset, we fill the gaps with linear interpolation. Images with a total of four or more erroneous lines are removed entirely.

To ensure temporal continuity, we enforce a maximum interval between subsequent images of 3 h, which is the nominal interval between full-disk images[1] and the minimum duration criterion we use for MCS identification.

[1] A full-disk scan by a geostationary satellite captures the entire hemisphere visible from the satellite's position in orbit. For the GOES satellites used in this study, full-disk scans nominally occurred at 3-h intervals, while scans specifically over North America or the continental United States occurred at more rapid frequencies. In the event of a schedule change, the more frequent scans may be cancelled, but the full-disk scan was typically conducted.

In the event of a data gap longer than 3 h, MCSs existing in either image bordering the data gap are removed because their lifetime is incomplete, and no MCS may contain a data gap within its duration.

The total coverage for the 1996–2017 period is 97.2%, but most of the missing times are in the first two years, which only have 86.7% (1996) and 75.9% (1997) coverage. All other years have greater than 95% coverage, and 16 of the 22 years have greater than 98% coverage. When considering the 22-yr record of each month, only March (90.8%) has less than 95% coverage.

b. *MCS identification and tracking*

For MCS identification and tracking, we implemented our own version of the area-overlap algorithm from Williams and Houze (1987). It is built on a graph database, as in Whitehall et al. (2015). A graph database is composed of *nodes* that are connected by *edges*. When applied to tracking MCSs, each node represents a cloud shield identified in a single image, and each edge connects the clouds from one image to the next. This technique was chosen for its ability to run without any human intervention once provided parameters. Machado et al. (1998) demonstrated that automated area-overlap techniques perform similarly to more sophisticated hybrid manual-automatic methods, but without the labor intensiveness.

Each satellite image of cloud top temperatures, called a *frame*, is masked at a temperature threshold of 221 K (−52°C). A contiguous area of cloud-top temperature colder than 221 K within a frame is a *cloud element* and saved to a node in the database. The areal extent is calculated for each element and stored as a property of its node. If there is an areal overlap of elements from subsequent images, an edge is added to connect the two nodes, indicating that the two elements represent the same system moving through time. This approach is successful in handling rapid growth, rapid decay, mergers, and splits. A potential MCS is represented as a *connected component* (all nodes that have a path to each other) in the graph database. Due to mergers and splits, it is common for a connected component to contain multiple elements in the same frame. A group of connected elements in the same frame is referred to as a *cloud cluster*. To meet the requirements for an MCS, the cloud clusters must maintain a size threshold for a continuous duration, which we take to be 30 000 km^2 for at least 3 h.

The temperature, size, and duration criteria used to identify MCSs are arbitrarily selected but based on previously published techniques. The 221 K temperature threshold has been used repeatedly for Great Plains MCS research, beginning with Maddox (1980), who used it alongside 241 K because these temperatures are easily identifiable contours on images that use the MB enhancement curve (a false-color enhancement for viewing infrared satellite images). Augustine and Howard (1988) argued for abandoning 241 K, as systems with separate 221 K cloud shields often share 241 K cloud shields if they are in close proximity. Subsequent satellite-based studies of MCSs over the Great Plains have used 221 K as the temperature threshold (e.g., Augustine and Howard 1988, 1991; Anderson and Arritt 1998, 2001; Jirak et al. 2003). The relationship between area and temperature threshold is nearly linear for changes on the order of 5–10 K (Mapes and Houze 1993). A relaxed threshold results in larger area and/or duration (Augustine and Howard 1988; Mapes and Houze 1993; Haberlie and Ashley 2018). Our own analysis of temperature threshold sensitivity similarly suggests that the overall results do not fundamentally change.[2]

Although we ultimately find that there is no clear threshold that separates MCSs by size and duration, the algorithm does require minimum size and duration criteria to consider the cloud cluster as an MCS. Our criteria were selected for consistency with previous work in the region. Maddox (1980) first established MCC criteria with 50 000 km^2 maintained for 6 h. Jirak et al. (2003) added complementary meso-β classes that used criteria of 30 000 km^2 maintained for 3 h, with the constraint that the maximum size must also be 50 000 km^2 or greater (Table 1). The 3 h time scale was selected to correspond with the inverse of the Coriolis frequency at midlatitudes, as suggested for mesoscale circulation (Emanuel 1986; Parker and Johnson 2000), and 30 000 km^2 corresponds approximately to a circle drawn with a 100 km radius, the length scale for radar-based convective lines recommended for MCS study (e.g., Houze 1993; Parker and Johnson 2000). We dropped the Jirak et al. (2003) requirement that maximum size exceed 50 000 km^2, but we found that 83.9% of systems that maintained 30 000 km^2 for 3 h still exceeded 50 000 km^2 at their maximum extent. Our preliminary analysis also tested various combinations of size and duration criteria, and we discuss this sensitivity in section 4.

c. *MCS processing*

The size of a cloud element is obtained by summing the areas of the pixels contained within the element.

[2] We also tested 211, 231, and 241 K. The differences in results by using the different thresholds have minimal impact on the analyses. For the more relaxed (warmer) thresholds, more smaller systems were identified, while larger systems often merged together. Systems that reached the edge of the domain were also far more common with relaxed thresholds.

TABLE 1. MCS classifications typically used in previous literature for regions of cloud-top temperatures colder than 221 K (−52°C).

Classification	Size	Duration	Reference
Mesoscale convective system (MCS)	≥30 000 km^2	≥3 h	This study
Mesoscale convective complex (MCC)	≥50 000 km^2	≥6 h	Augustine and Howard (1988)
Persistent elongated convective system (PECS)	≥50 000 km^2	≥6 h	Anderson and Arritt (1998)
Meso-β circular convective system (MβCCS)	≥30 000 km^2 Max ≥ 50 000 km^2	≥3 h	Jirak et al. (2003)
Meso-β elongated convective system (MβECS)	≥30 000 km^2 Max ≥ 50 000 km^2	≥3 h	Jirak et al. (2003)

The area of a cloud cluster is the sum of the sizes of its elements. Maddox (1980) uses the terms *initiation*, *maximum extent*, and *termination* to describe the moments when the MCS first exceeds the size criterion, when it reaches maximum size, and when it first falls below the size criterion. We estimate the times of initiation and termination by linearly interpolating between frames. The duration of an MCS is the time elapsed between initiation and termination. If a potential MCS component has two distinct periods in which its area meets the minimum size requirement, separated by a period of time during which it does not, the component is split at the time of minimum area and each newly separate component is considered independently in all previous and subsequent calculations.

For time-of-day analysis, we use central daylight time (CDT), which equals UTC − 5 h. This time was chosen to coincide with the greatest activity across the domain during the most active season. When a system needs to be assigned to a day of the year, we use the day on which it initiated, even if it survives to the next day (which is common). Location is determined by both the center of mass of each cloud cluster and by the entire area covered by a cloud cluster. The center of mass location is used for system motion calculations, while cloud cover areas are used for map-based calculations.

We are interested in the domain bounded by 27.5°–52.5°N and 77.5°–107.5°W because it captures MCS activity over the Great Plains and the Deep South, the most active regions (HA19; F19). To minimize the impact of the domain boundaries on the analysis, we process the domain of interest within a larger region, bounded by 20°–55°N and 65°–115°W. This larger region allows us to capture the full lifetime information of most MCSs that occur within the domain of interest even if they are only within the domain for a short time. Our selected domain of interest frequently captures MCSs associated with the North American monsoon, which we excise because they occur near the edge of the GOES-East coverage and would be better studied by GOES-West imagery. To remove their influence on our composites, we eliminate the southwest corner (bounded by a line from 32.5°N, 107.5°W to 27.5°N, 102.5°W) from the domain of interest and remove MCSs that exist only within this corner. Also, we use precipitation-type output from ERA5 reanalysis (Copernicus 2017) to identify and remove systems which contain nonhail frozen precipitation. If an MCS occurs within the larger region and does not enter the domain of interest, it is not included in the analysis. Similarly, if an MCS reaches the outer edge of the larger domain, it is removed from analysis because we have incomplete information on that MCS. By removing the systems on the outer edge of the domain, we also effectively remove tropical cyclones from the dataset. We discuss the impact of the domain on the results in section 3.

We assert that we have the complete life cycle of the MCS if we have its entire spatial information (i.e., the MCS does not touch the outer edge of the larger domain) and temporal information (i.e., the MCS duration does not contain a data gap). We identify 9607 MCSs that meet these criteria, and compare MCS life cycles at the same moments in their evolution. We end up comparing systems of vastly different duration, but find that life cycles follow remarkably similar patterns regardless of duration.

Regional analyses are only conducted on subsets of the data that pass within a 5° box of the Plains or Deep South grid cells with maximum frequency (the geographic modes). After removing the 218 MCSs that are shared by the two modes, 2028 MCSs comprise the PL subset, and 1714 comprise the DS subset. The analyses performed on these subsets are otherwise the same as those performed on the entire domain.

3. Spatial and temporal characteristics

Previous studies have identified favorable baroclinicity, wind shear, and CAPE as reasons that the central and southeastern United States is one of the most active locations for MCSs (e.g., Laing and Fritsch 1997, 2000). These ingredients are typically provided by common synoptic-scale phenomena such as baroclinic fronts

(Maddox 1983) and the Great Plains LLJ (Trier and Parsons 1993). Given enough warm, moist air in the lower levels, however, MCSs also often develop with only smaller, local initial forcings (S19; F19). This shifts the typical favorable MCS ingredients to the local scale in summer from the synoptic scale the rest of the year. Regardless of the environmental scale, MCSs are strongly modulated diurnally, as both the synoptic-scale LLJ and the local forcings (such as the MPS or a land–sea breeze) have diurnal recurrence (Blackadar 1957; Holton 1967; Tian et al. 2005).

a. Seasonal cycle

Frequency per grid cell (0.025°) is determined by counting the number of MCS cloud shields that affect that cell (Fig. 1). We observe maximum MCS frequency in PL, with an average of 32.5 MCSs per year in grid cells near 40°N, 95°W. The spatial distribution of frequency resembles a bull's-eye that stretches across the center of the continent. The broad area of grid cells averaging more than 20 MCSs per year spans a radius greater than 750 km and contains much of the central and southeastern United States. This PL maximum agrees with the warm-season MCS studies (e.g., Ashley et al. 2003).[3]

We also observe a local maximum of MCS frequency along the coastline in the DS, but this maximum is of a lesser magnitude than PL. The DS gridcell maximum annual frequency is 25.4 MCSs (or 78% of PL) near 31°N, 90°W, and is separated from the larger bull's-eye pattern to its northwest by a local minimum at 33°N, 91°W (20.9 MCSs per year). To conduct detailed analysis of these two regional modes, we define 5° boxes around the locations of local maximum for each. In these regional analyses, we consider the subsets of MCSs that pass through each 5° box. This creates subsets of 2028 MCSs in PL and 1714 in DS (after removing the 218 that passed through both).[4]

Many previous studies focused on the warm season, when MCSs are most frequent (e.g., Bartels et al. 1984; Augustine and Howard 1988, 1991; Anderson and Arritt 1998, 2001; Ashley et al. 2003). They also find that during the warm season, MCSs are most common near PL. In studies that examine the entire year (e.g., HA19; F19), MCSs are found in and near DS throughout winter,

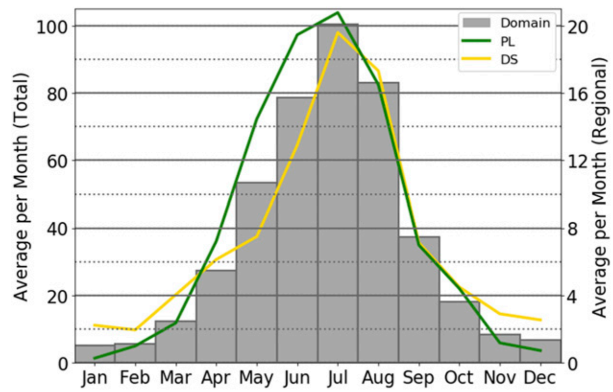

FIG. 2. Mean annual MCS counts by month. Histogram represents entire domain (left *y* axis). Green and yellow lines represent Plains (PL, green) and Deep South (DS, yellow) modes, respectively (right *y* axis).

which extends the area of high annual frequency toward the south.

We find a strong seasonal cycle with a 20-fold decrease in magnitude between the maximum monthly frequency (July, 100.5) and the minimum (January, 5.1; Fig. 2). While June (78.7) and August (83.1) frequencies reach near 80% of the July maximum, we observe an asymmetry between spring and autumn in that MCS frequency increases more gradually in spring, taking 18 weeks to increase from mid-March levels (2.5 per week) to the maximum in mid-July (23.2 per week). In contrast, it takes 3 fewer weeks in the autumn for the frequency to return to 2.5 per week in mid-November.

This seasonal pattern qualitatively agrees with HA19 and F19, but the differences are noteworthy. Both papers report less contrast between the maximum in June and minimum in January (a factor of 9 and 12 in HA19 and F19, respectively, cf. our 20), while frequencies in May, July, and August are somewhat larger (80%–90% vs 70%–80%). The latter difference makes their monthly averages more symmetric around June and July. The discrepancy may arise from the choice of identification and tracking techniques. For example, in our tests of different temperature thresholds, warmer temperature thresholds result in larger relative frequencies in fall and winter, while colder thresholds result in relatively larger frequencies in spring[5] (Figs. S3, S4 in the online supplemental material). Furthermore, strong radar reflectivity (e.g., ≥40 dBZ) is more frequent in DS than elsewhere in the domain (Fairman et al. 2016).

[3] We tested whether the bull's-eye pattern is an artifact of the limited domain by considering how MCS frequency changes with the inclusion of MCSs that occurred on the edge of the domain (Fig. S1). Even with these MCSs included, the bull's-eye is fundamentally unchanged.

[4] The heatmaps associated with MCSs that pass through each box are provided in Fig. S2.

[5] If a temperature threshold of 241 K is used, there is only a 14-fold difference between monthly maximum (July) and minimum (December) frequency, but with frequencies relatively higher in the fall and lower in the spring.

The locations of MCS occurrence are also strongly tied to the seasonal cycle. The most active region for MCS occurrence varies from PL in the summer to DS in the winter. While our observations agree with HA19 and F19 in that winter MCSs occur most commonly in DS, we detect many fewer winter MCSs. In the average DJF, the grid cells with the highest frequency (in and around DS) only observe two MCSs (Figs. S4, S5). As a result, our annual frequency pattern across all regions is primarily driven by summer and spring. In March and April, MCSs begin to occur more frequently over the northern part of DS. As the season changes to summer, MCS frequency continues to increase and migrate to the northwest, following the typical migration of the NASH (Li et al. 2012). In June, MCSs are most common in PL and to its west, but an increase in occurrence also begins along the DS coast. These two regional maxima persist in July and August, ultimately creating the two regional modes observed in the annual frequency map (Fig. 1). In September, MCSs become much more scarce, and by November, MCSs are essentially restricted to in and around DS (Fig. S6).

The relationship between geography and season is also demonstrated by comparing the two geographic modes (Fig. 2). From November to March, DS experiences more than twice as many MCSs as PL. As the thermodynamic profiles are typically more stable in the winter, it follows that MCSs would be restricted to near the Gulf of Mexico, where proximity to warm water keeps convective instability relatively higher when compared to the plains. From April through June, frequency in PL quickly increases, outpacing the frequency in DS by as much as 7 MCSs (more than two times as many) per month. This rapid increase in frequency corresponds with the seasonal NASH migration (Li et al. 2012) and increased LLJ occurrence in PL (Weaver and Nigam 2008). In July, PL and DS both reach maximum. At this time, however, DS is dominated by smaller and shorter-lived MCSs (shown in section 4d) that suggest smaller-scale disturbances as the triggers for initiation (as suggested by F19 and S19). The two modes' frequencies then decrease together throughout autumn.

System movement patterns are an influential factor in MCS climatology and also vary by season and location. Individual MCSs persist for many hours and can travel several hundreds of kilometers during their lifetime. Some locations that most commonly observe MCSs are also regions where they rarely initiate (e.g., the eastern plains), which means that their climatology is dominated by MCSs that develop upstream. We find that most MCSs (82%) move east after initiation, which is consistent with climatological synoptic wind patterns.

To further examine MCS movement, we examine the median paths taken by MCSs after their initiation

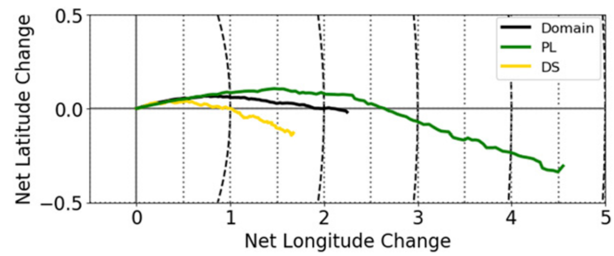

FIG. 3. Paths of regional composite MCSs relative to the initiation location in degrees latitude and longitude for the overall domain (black), Plains (PL, green), and Deep South (DS, yellow).

(Fig. 3). Median paths follow an anticyclonic arc, first traveling to the east before eventually turning southeast. Compared to the domain average, PL MCSs tend to travel farther to the east before turning south, while DS MCSs cover less distance and almost immediately turn to the southeast. This result is consistent with the typically longer durations of PL MCSs (shown in section 4d) and differences in the synoptic-scale environments that lead to MCSs in the two regions.

Using the same domain-based composites, we also calculate the typical movement speeds throughout the system lifetime (Fig. 4). Ignoring the artifacts at the beginning and end of MCS lifetime,[6] we see the average movement speed slightly increase from 13 to 15 $\mathrm{m\,s^{-1}}$ as the MCSs age. The range of movement speed remains consistent throughout MCS lifetime, with the MCSs moving between roughly 5 and 30 $\mathrm{m\,s^{-1}}$ (10th–90th percentiles). These values are in agreement with F19, who calculated MCS movement speeds from 6 to 30 $\mathrm{m\,s^{-1}}$, and Carbone et al. (2002), who identified phase speeds of 7–30 $\mathrm{m\,s^{-1}}$ consistent with a combination of steering wind advection and cold pool propagation. Between the regional modes, DS averages 1 $\mathrm{m\,s^{-1}}$ slower than the full domain median, while PL averages 2.5 $\mathrm{m\,s^{-1}}$ faster.

b. Diurnal cycle

MCS frequency is heavily modulated by the diurnal cycle. Given the importance of MCSs in the climate system and the modeling community's difficulties in simulating many aspects of this cycle (e.g., Prein et al. 2017), properly simulating the diurnal behavior of MCSs and their ingredients (e.g., LLJ) will likely lead to better simulations of the entire climate. The diurnal pattern of propagating precipitation across the continent is well documented in the region, and MCS movement aligns

[6] The appearance and disappearance of new and old elements cause jumps in the algorithm's calculation of the cluster's center of mass.

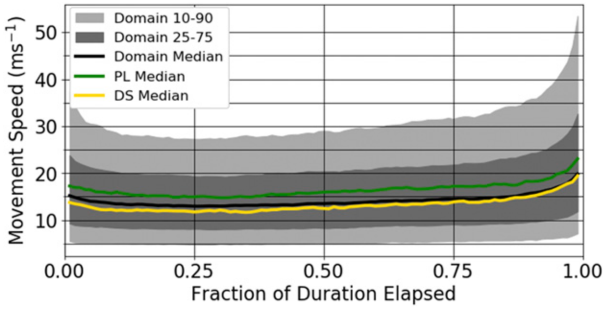

FIG. 4. Movement speed of regional composite MCSs as a function of duration elapsed for overall domain (black), Plains (PL, green), and Deep South (DS, yellow).

extremely well with the warm season precipitation patterns (e.g., Carbone and Tuttle 2008).

Our observed diurnal pattern of MCS frequency follows that of other MCS studies (e.g., Maddox 1980; Bartels et al. 1984; Augustine and Howard 1988; Anderson and Arritt 1998; Jirak et al. 2003), (HA19; F19), in that MCSs are most frequent in the late evening and least frequent around noon (Table 2). We find that MCSs are most common at 2000 CDT, during which 60.6% of all MCSs are active, compared to the least common time of 1100 CDT, during which only 24.5% are active.

The two regional modes are quite different in their diurnal patterns (Fig. S7). MCS frequency begins to increase along the coast in DS just after noon, then spreads into the rest of DS, reaching maximum at 1700 CDT. Around this time, a separate region of MCS activity begins in the west. This western region of activity quickly expands across PL, reaching its maximum at 2100 CDT. At the same time, MCS frequency in DS collapses, reaching minimum shortly after midnight. The region of high frequency in PL continues to propagate and slowly diminish throughout the early morning, reaching its minimum just after noon.

MCS initiations primarily occur within a small range of times. Half of all MCSs initiate during the 6 h from 1400 to 2000 CDT, with over 20% initiating in the 2 h between 1500 and 1700 CDT. The PL and DS times of initiation are similarly compact, with half of the MCSs in these regions also initiating within 6 h (1400 to 2000 CDT and 1200 to 1800 CDT, respectively). The preferred times of maximum extent and termination then occur throughout the night, and are not as compact due to the variations in system duration (Table 3).

There are two distinct prime locations for MCS initiation, each corresponding to one of the regional modes of maximum frequency. Although PL experiences the most MCSs, on average, it is relatively rare for these MCSs to initiate within PL. Instead, they typically initiate to the west, along the Rocky Mountain foothills,

TABLE 2. Hours (in CDT) of the maximum and minimum overall frequency.

Region	Maximum	Minimum
Overall	2000	1100
Plains	2100	1400
Deep South	1700	0200

and propagate eastward into PL. The other common initiation region is along the coast of the DS. Because DS MCSs typically do not move as far as PL ones, most of these MCSs remain in DS for their duration (Figs. 5, S8).

4. Duration and size

MCS duration and size are the main defining criteria in most satellite-based studies (e.g., Maddox 1980; Augustine and Howard 1988; Anderson and Arritt 1998; Jirak et al. 2003). The largest and longest-lasting MCSs have an outsize impact on the climate system, not only because they affect larger areas for longer amounts of time (contributing substantially to the local precipitation budgets), but also because of the increased upscale impacts that larger, longer-lasting MCSs have on the synoptic environment (e.g., Yang et al. 2017). The top-heavy vertical profile of diabatic heating generates a positive midlevel potential vorticity anomaly (Fritsch et al. 1994), called a mesoscale convective vortex (MCV), that can exist well after its generative MCS has dissipated (Johnston 1981; Bartels and Maddox 1991). MCVs are strengthened by larger and longer-lasting MCSs, and in turn, they enable both the persistence of the generative MCS and the initiation of future MCSs. On the other hand, smaller and shorter-lasting MCSs have been found to be exponentially more common (e.g., Jirak et al. 2003; Yang et al. 2017; Song et al. 2019). Due to their numbers, their impacts cannot be discounted.

a. *Distributions*

While the exact distributions of duration and maximum size are dependent on the identification criteria, it is much more common for MCSs to be smaller and short-lived. The distribution of maximum size is the most sensitive to the criteria because the duration

TABLE 3. Hours (in CDT) of most common initiation, maximum extent, and termination.

Region	Initiation	Maximum extent	Termination
Overall	1500 (10%)	1800 (9%)	2100 (7%)
Plains	1700 (11%)	2300 (9%)	0900 (8%)
Deep South	1400 (13%)	1700 (13%)	2100 (9%)

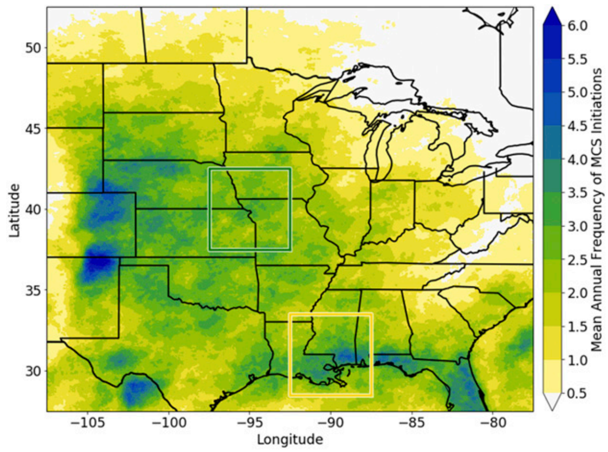

FIG. 5. As in Fig. 1, but for locations of MCS initiations.

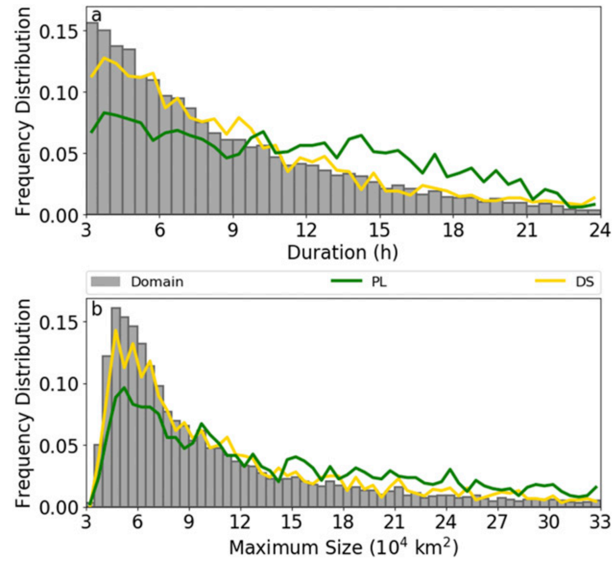

FIG. 6. Frequency distributions of MCS (a) duration and (b) maximum size for the entire domain (histogram), Plains (PL, green), and Deep South (DS, yellow).

requirement dampens the frequency of the very smallest MCSs (Fig. 6). In order for an MCS to maintain the minimum size threshold for the time required, the lifetime maximum size must overshoot the minimum threshold by a factor that depends on the duration criterion. For example, a change in duration criterion from 3 to 6 h moves the median maximum size from 79 000 to 115 000 km^2 (Fig. S9). The reduction in frequency of the smallest MCSs caused by longer-duration criterion results in a maximum size distribution appearing closer to lognormal.

The differences between PL and the rest of the domain are illustrated by the patterns of duration and size. (Fig. 6, Tables 4 and 5). PL averages much longer durations and larger maximum sizes than DS and the full domain. The distributions in PL are less skewed and much flatter. PL duration decreases almost linearly, as opposed to exponentially (as seen in DS and domain average), and the maximum size, while still appearing lognormal, has a much heavier tail. Conversely, duration and maximum size in DS are quite similar to overall, with only a subtle deviation in that the distribution of maximum size is slightly flatter than in the entire domain (as can be seen by comparing kurtosis).

Because the duration and maximum size distributions exist on continua in which frequency decays quickly but smoothly as either characteristic increases, there are no obvious duration or size thresholds upon which to base a satellite-based classification. Jirak et al. (2003) noted that the choice of subclassifying criteria can prejudice the interpretation of results. In dividing MCSs into two categories based on criteria (see Table 1) close to the overall minimum requirement, they identified more MCSs in the larger and longer-lasting category, even though they found distributions of duration and maximum size that decay quickly as the parameters increase. We see the same sensitivity to these thresholds (Fig. 6). The satellite data alone do not suggest an obvious scheme for subclassifying MCSs based on duration and size.

b. *Seasonal cycle of duration and size*

Distributions of maximum size and duration also change from spring to summer. This is best illustrated by their cumulative distributions (CDFs, Fig. 7). May and June (MJ) are examined together, because they are qualitatively similar, and we combine July and August (JA) for the same reason. The CDFs of MJ and JA are nearly identical at the smallest sizes and durations. They then diverge, reaching a maximum at 12 h and 200 000 km^2. Thus, the MCSs in the middle range of values are relatively more common in JA than MJ and systems larger than 12 h and 200 000 km^2 are more common in MJ than JA. The greater significance of smaller, shorter-lived MCSs in JA compared to MJ is further support for F19 and S19's suggestion that locally forced MCSs are more common in summer.

The differences between PL and the rest of the domain is also evident in Fig. 7. While CDFs of DS and

TABLE 4. Summary statistics for the distributions of duration.

	Mean (h)	Median (h)	Mode (h)	Std dev (h)	Skewness	Kurtosis
Overall	9.3	7.2	3.0–3.5	7.0	3.56	26.69
Plains	12.2	11.1	3.5–4.0	7.4	1.72	6.17
Deep South	9.6	7.5	3.5–4.0	7.5	3.65	24.60

TABLE 5. Summary statistics for the distributions of maximum size.

	Mean (10^4 km^2)	Median (10^4 km^2)	Mode (10^4 km^2)	Std dev (10^4 km^2)	Skewness	Kurtosis
Domain	11.4	7.9	4.5–5.0	9.5	2.65	9.46
Plains	17.6	13.0	5.0–5.5	13.4	1.59	3.06
Deep South	10.8	8.3	4.5–5.0	7.4	2.17	6.45

overall domain both quickly asymptotically approach 100%, PL does so much more gradually. This means that the largest and longest-lasting MCSs are a much more significant component of climatology in PL than in DS or the full domain. Seasonally, the largest separation between MJ and JA duration CDFs are also 12 h for both regional modes. Substantially different are the sizes at maximum separation, which occur at 90 000 km^2 in DS and 270 000 km^2 in PL. This indicates that the seasonal variations in duration occur at roughly the same scales regardless of location; meanwhile, those seasonal variations in maximum size are influenced by location.

The influence of seasonal changes can also be seen in the spread of duration and size within each month (Fig. 8), particularly in the median and upper quartile (the lower quartile changes little throughout the year). The medians for duration and maximum size are largest in the late spring, and duration exhibits a secondary maximum in the fall. The medians for DS also show bimodality in the transition seasons, particularly for duration, whereas PL has only a single mode in each characteristic (MJ). Throughout the summer, the median size and duration of PL MCSs are equal to or greater than the 75th percentiles of the entire domain. When DS MCSs are at their smallest and shortest lasting, PL commonly experiences some of the largest and longest-lasting MCSs in the entire United States.

c. Duration-size correlation

To quantify the correlation between duration and maximum size, we calculate both Pearson (testing for linearity) and Spearman (testing for monotonicity) correlation coefficients, obtaining values of $\rho = 0.71$ and $r = 0.83$, respectively. Recognizing the exponential nature of the size and duration distributions, we also performed the Pearson test on the natural logarithms of duration and maximum size (0.82). These tests all indicate that there is a strong positive correlation between duration and maximum size.

This strong correlation can be seen in Fig. 9. As both duration and maximum size are distributions that decay exponentially, most observed MCSs fall into the category of small and short lived. As longer durations are considered, the envelope of observed maximum sizes expands but still increases monotonically. For the shortest durations, very large MCSs are extremely rare. Similarly, small MCSs are rare for the longest durations. The extreme durations are slightly more rare in DS and slightly less rare in PL.

d. Life cycle of size

Using the same location-based composites as in section 3a (Fig. 4), we examine the patterns of size throughout the MCS lifetime (Fig. 10a). For each composite, the systems are compared at equal percentages of duration elapsed. We calculate statistics as a function of this normalized duration. This approach simplifies the climatology to a smooth function of time that closely follows a parabola. The average of DS closely resembles the median for the entire domain, while PL exhibits a much larger average size than the overall domain. This is partially due to the tendency for PL MCSs to have longer durations, but is also due to their larger initial growth rates.

The average growth rates throughout the system life cycle are calculated in the same manner as system size (Fig. 10b). Consistent with the parabolic shape of the

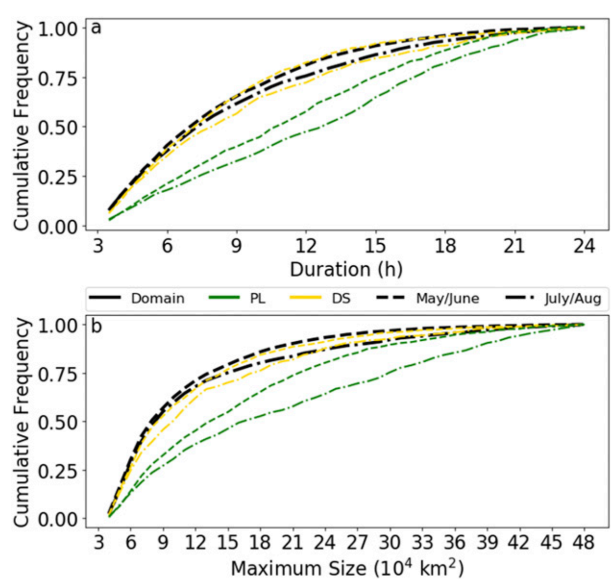

FIG. 7. Cumulative distribution functions of (a) duration and (b) maximum size for the entire domain (black), Plains (PL, green), and Deep South (DS, yellow). The May/June distributions are drawn with dashed lines, while July/August distributions are dash–dotted.

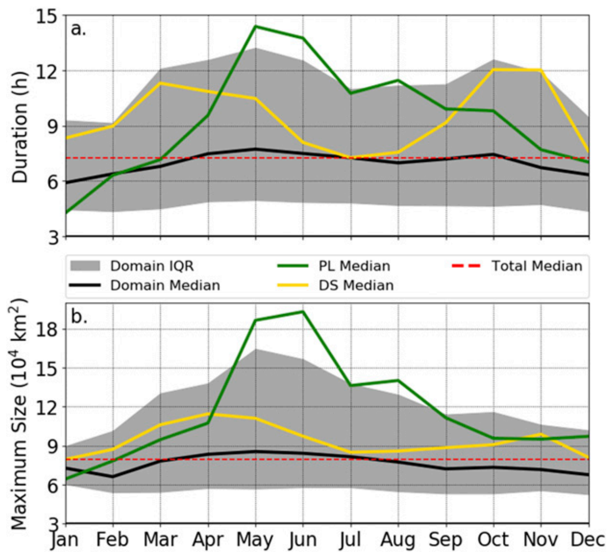

FIG. 8. Distributions of median (a) duration and (b) maximum size of MCSs, by month for the overall domain (black), Plains (PL, green), and Deep South (DS, yellow). The 25th to 75th percentile for the overall domain (shaded) and the median for the entire dataset (red dashed line) are also illustrated.

time series for size, composite growth rates are at their maximum at the time of initiation and decrease near-linearly with time. These average growth rates reach zero just after 50% of the total duration. Again, the average of DS closely resembles the domain median, while PL MCSs typically have greater initial growth rates.

The parabolic model for the composite life cycles is written as

$$S(t) = S_0 + G_0 t + G' t^2/2, \qquad (1)$$

where t is the time since initiation, S is system size, S_0 is initial size (we use 30 000 km^2), G_0 is initial growth rate, and G' is the rate at which the growth rate changes, averaged over the life cycle. To align with Fig. 10, where we are interested in the percentage of the duration elapsed, we introduce nondimensional time as $\tilde{t} = t/D$, where D is system duration. We also define $\tilde{G}_0 = G_0/D$ and $\tilde{G}' = G'/D^2$. Then we can state (1) as

$$\Delta S(\tilde{t}) = \tilde{G}_0 \tilde{t} + \tilde{G}' \tilde{t}^2/2, \qquad (2)$$

where $\Delta S = S - S_0$, as plotted in Fig. 10a. Furthermore, because $\Delta S(0) = \Delta S(1) = 0$, we obtain $\tilde{G}' = -2\tilde{G}_0$. Substituting this into (2) simplifies the function to

$$\Delta S(\tilde{t}) = \tilde{G}_0 \tilde{t}(1 - \tilde{t}). \qquad (3)$$

The empirically calculated values of $\tilde{G}_0$ for each composite (Table 6) show that G_0 is similar for DS and

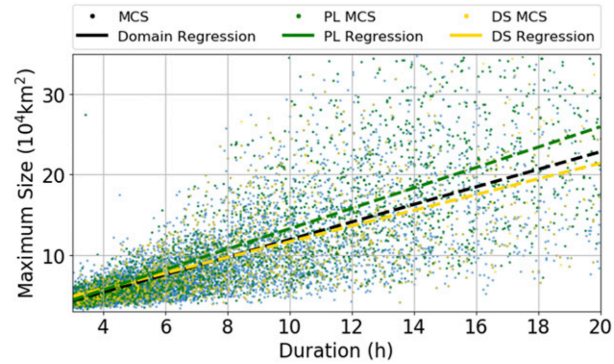

FIG. 9. Scatterplot of duration and maximum size for the entire domain (black), Plains (PL, green), and Deep South (DS, yellow). Individual MCSs (points) and regional linear regressions (dashed lines) are illustrated.

the domain, but much larger in PL, even after normalizing by D. Thus, the longer-lived MCSs from PL also tend to have a larger initial growth rate.

5. Discussion and conclusions

In this paper, we have provided a 22-yr climatology of the spatial and temporal characteristics of 9607 MCSs in the central and southeastern United States, compiled

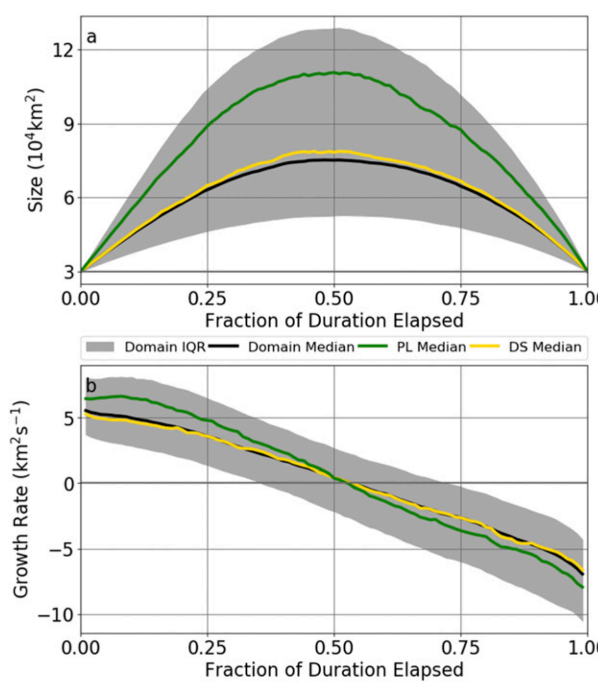

FIG. 10. (a) Size and (b) growth rate of MCSs as a function of time since MCS initiation for overall domain (black), Plains (PL, green), and Deep South (DS, yellow). The 25th to 75th percentile for the overall domain (shaded) is also illustrated.

TABLE 6. Estimates of $\tilde{G}_0$ for each region, as determined by fitting Eq. (3) to the median life cycles of size for the composites in Fig. 10a. Values for G_0 are estimated by dividing the fitted $\tilde{G}_0$ by the median duration.

	$\tilde{G}_0$ (10^4 km^2)	Median D (h)	G_0 (km^2 s^{-1})
Domain	16.0	7.2	6.2
Plains	30.3	11.1	7.6
Deep South	16.6	7.5	6.1

from geostationary satellite images. We implemented an automated identification and tracking algorithm on a single data source, which ensures that the constructed dataset is self-consistent. The resolution and expansiveness of this dataset allowed for detailed analyses that highlight the evolution throughout MCS lifetimes and the differences between the two regional modes.

Environmental conditions favorable for MCS development have previously been identified as low static stability, CAPE, a baroclinic frontal zone, vertical wind shear, low-level convergence, and upper-level divergence (Maddox 1983; Burke and Schultz 2004; Laing and Fritsch 1997, 2000; Coniglio et al. 2010; Yang et al. 2017; F19; S19). MCSs are typically associated with a LLJ, which provides low-level advection of θ_e (equivalent potential temperature) and vertical wind shear (Peters and Schumacher 2014). The climatological maximum temperature and humidity in summer allow for MCSs to initiate with local forcings, even in the absence of favorable synoptic-scale conditions (F19; S19). In these instances, a local forcing such as a bore (Geerts et al. 2017; Parsons et al. 2019; Haghi et al. 2019), the MPS or a sea breeze can provide sufficient lift, but without additional larger-scale forcing, these MCSs typically remain small (Yang et al. 2017). Despite the different initiation mechanisms, MCS duration and maximum size patterns exist on a continuum, and we find no obvious scheme to classify MCSs based on satellite patterns alone.

Although MCSs can initiate without favorable large-scale environments, their size and longevity are dependent on the large-scale environment. The largest and longest-lasting MCSs typically occur in the presence of a strong, broad LLJ and/or large-scale lift in advance of a trough (Maddox 1983; F19). Among the longest-lived MCSs, the top-heavy heating profile generates potential vorticity anomalies (Maddox 1980; Raymond and Jiang 1990; Fritsch et al. 1994; Stensrud 1996; Li and Smith 2010; Yang et al. 2017). These create upscale feedbacks that influence large-scale circulations, encourage further MCS maintenance, and aid future MCS initiation.

We find that MCSs in the plains represent the primary regional mode, where individual grid cells average up to 32.5 MCSs per year. During the warm season, PL commonly receives additional warm, moist air and vertical wind shear from the LLJ (Coniglio et al. 2010; Peters and Schumacher 2014). Synoptic-scale troughs also regularly cross PL, but are strongest in the spring (F19). PL MCSs typically initiate in the afternoon, often along the eastern slope of the Rocky Mountains. These first storms are consistent with locally forced lift from the MPS. Further evidence for this initiation mechanism is the absence of MCS initiation directly over PL during the afternoon (Weckwerth and Romatschke 2019), as the MPS causes a sinking motion over PL in the afternoon (Tian et al. 2005; Carbone and Tuttle 2008). As a result, PL MCSs typically enter PL later in the night, as they travel along an eastward anticyclonic arc.

PL MCS frequency increases rapidly through the spring. At the end of spring, the typical PL MCS is among the largest and longest lasting to occur in the United States. During this time, low-level temperature and humidity are approaching their climatological maximum, providing ample potential energy for convection. Synoptic-scale baroclinic troughs are at their strongest during this time (Wang and Chen 2009; Feng et al. 2016), as is the LLJ (Weaver and Nigam 2008; Weaver et al. 2009). Springtime initiations also occur closer to PL, indicating that spring initiations are dominated by synoptic, rather than local, forcings.

Seasonal frequency in PL maximizes in July, which averages nearly 18 MCSs. Due to the summertime maximum in temperature and humidity, the Rocky Mountain foothill climatological environment is conducive enough that local forcing from the MPS is enough to initiate an MCS (S19). Even though an MCS can initiate with locally driven lifting, the large-scale environment must still be favorable; otherwise, the MCS will remain small and short lived (Yang et al. 2017; F19; S19). This is illustrated by the decrease in median duration and maximum size that occurs in the summer, corresponding with maximum frequency.

Meanwhile, the Deep South experiences the secondary regional mode, where the most active grid cells average 25 MCS in an average year. The lower latitude and proximity to warm water in the Gulf of Mexico make DS warmer and more humid than the rest of the domain (Tian et al. 2005). As a result, the climatological mean conditions are conducive for locally forced MCS initiation for a longer period of summer. This is evidenced by the smaller median duration and maximum size that occurs along with maximum frequency from May through August. The largest and longest-lasting MCSs occur earlier in spring, in April and March, respectively. There is also a secondary maximum in duration and maximum size in fall, which suggests similarity of the transition seasons (F19). Even in winter, the warm, humid air from the Gulf of Mexico couples with favorable synoptic environments for MCS initiation. Although we do not observe as many winter MCSs as HA19 and F19 (likely due to different identification schemes), we do agree that winter MCSs are typically confined to in and around DS.

The local forcing in DS is associated with the land–sea breeze (Tian et al. 2005), shown by initiations occurring along the coast. Because DS is to the east of the Rockies, the diurnally forced initiations occur earlier in the afternoon by a couple hours. Also, because DS MCSs more commonly occur in weaker mean flows, they tend to move more slowly and travel less distance.

Beyond the regional differences, we found duration and maximum size to be strongly correlated. The lifetime of MCS sizes closely follow a parabolic evolution in which growth rate and its decrease over time combine to produce the size-duration correlation. While this does not apply generally to all MCSs, it does robustly represent the average MCS lifetime pattern.

More broadly, accurately representing the spatial and temporal patterns of MCSs will become critical as climate models become more sophisticated. For example, a dry bias commonly occurs in models of the central United States (Dai et al. 1999; Prein et al. 2017; F19). This is likely due to poor representation of diurnal MCSs propagation across the Plains (Tian et al. 2005). The climatology presented in this paper, along with the techniques for summarizing MCS climatology, provide modelers and theorists resources with which to compare their models.

Acknowledgments. We are grateful to Kim Whitehall for guidance in modifying her algorithm for our purposes, and to Leo Donner for his constructive suggestions during the early stages of this study. Thoughtful reviews by Lucas Harris, John Lanzante, David Schultz, and three anonymous reviewers resulted in significant improvements to the manuscript. We are also appreciative of the technical guidance provided by Spencer Clark. This report was prepared by Shawn M. Cheeks under Award NA18OAR4320123 from the National Oceanic and Atmospheric Administration, U.S. Department of Commerce. The statements, findings, conclusions, and recommendations are those of the author(s) and do not necessarily reflect the views of the National Oceanic and Atmospheric Administration, or the U.S. Department of Commerce.

REFERENCES

Anderson, C. J., and R. W. Arritt, 1998: Mesoscale convective complexes and persistent elongated convective systems over the United States during 1992 and 1993. *Mon. Wea. Rev.*, **126**, 578–599, https://doi.org/10.1175/1520-0493(1998)126<0578:MCCAPE>2.0.CO;2.

——, and ——, 2001: Mesoscale convective systems over the United States during the 1997–98 El Niño. *Mon. Wea. Rev.*, **129**, 2443–2457, https://doi.org/10.1175/1520-0493(2001)129<2443:MCSOTU>2.0.CO;2.

Ashley, W. S., T. L. Mote, P. G. Dixon, S. L. Trotter, E. J. Powell, J. D. Durkee, and A. J. Grundstein, 2003: Distribution of mesoscale convective complex rainfall in the United States. *Mon. Wea. Rev.*, **131**, 3003–3017, https://doi.org/10.1175/1520-0493(2003)131<3003:DOMCCR>2.0.CO;2.

Augustine, J. A., and K. W. Howard, 1988: Mesoscale convective complexes over the United States during 1985. *Mon. Wea. Rev.*, **116**, 685–701, https://doi.org/10.1175/1520-0493(1988)116<0685:MCCOTU>2.0.CO;2.

——, and ——, 1991: Mesoscale convective complexes over the United States during 1986 and 1987. *Mon. Wea. Rev.*, **119**, 1575–1589, https://doi.org/10.1175/1520-0493(1991)119<1575:MCCOTU>2.0.CO;2.

Bartels, D. L., and R. A. Maddox, 1991: Midlevel cyclonic vortices generated by mesoscale convective systems. *Mon. Wea. Rev.*, **119**, 104–118, https://doi.org/10.1175/1520-0493(1991)119<0104:MCVGBM>2.0.CO;2.

——, J. M. Skradski, and R. D. Menard, 1984: Mesoscale convective systems: A satellite-data-based climatology. NOAA Tech. Memo. ERL ESG-6, Environmental Research Laboratories, NTIS PB85-187862, 58 pp.

Blackadar, A. K., 1957: Boundary layer wind maxima and their significance for the growth of nocturnal inversions. *Bull. Amer. Meteor. Soc.*, **38**, 283–290, https://doi.org/10.1175/1520-0477-38.5.283.

Blamey, R. C., and C. Reason, 2012: Mesoscale convective complexes over southern Africa. *J. Climate*, **25**, 753–766, https://doi.org/10.1175/JCLI-D-10-05013.1.

Burke, P. C., and D. M. Schultz, 2004: A 4-yr climatology of cold-season bow echoes over the continental United States. *Wea. Forecasting*, **19**, 1061–1074, https://doi.org/10.1175/811.1.

Carbone, R., and J. Tuttle, 2008: Rainfall occurrence in the US warm season: The diurnal cycle. *J. Climate*, **21**, 4132–4146, https://doi.org/10.1175/2008JCLI2275.1.

——, ——, D. Ahijevych, and S. Trier, 2002: Inferences of predictability associated with warm season precipitation episodes. *J. Atmos. Sci.*, **59**, 2033–2056, https://doi.org/10.1175/1520-0469(2002)059<2033:IOPAWW>2.0.CO;2.

Carvalho, L. M., and C. Jones, 2001: A satellite method to identify structural properties of mesoscale convective systems based on the maximum spatial correlation tracking technique (MASCOTTE). *J. Appl. Meteor.*, **40**, 1683–1701, https://doi.org/10.1175/1520-0450(2001)040<1683:ASMTIS>2.0.CO;2.

Coniglio, M. C., J. Y. Hwang, and D. J. Stensrud, 2010: Environmental factors in the upscale growth and longevity of MCSS derived from rapid update cycle analyses. *Mon. Wea. Rev.*, **138**, 3514–3539, https://doi.org/10.1175/2010MWR3233.1.

Copernicus, 2017: ERA5: Fifth generation of atmospheric reanalyses of the global climate. Copernicus Climate Change Service Climate Data Store (CDS), accessed 7 September 2019, https://cds.climate.copernicus.eu/cdsapp#!/home.

Cotton, W. R., G. D. Alexander, R. Hertenstein, R. L. Walko, R. L. McAnelly, and M. Nicholls, 1995: Cloud venting—A review and some new global annual estimates. *Earth-Sci. Rev.*, **39**, 169–206, https://doi.org/10.1016/0012-8252(95)00007-0.

Dai, A., F. Giorgi, and K. E. Trenberth, 1999: Observed and model-simulated diurnal cycles of precipitation over the contiguous United States. *J. Geophys. Res.*, **104**, 6377–6402, https://doi.org/10.1029/98JD02720.

Durkee, J. D., and T. L. Mote, 2010: A climatology of warm-season mesoscale convective complexes in subtropical South America. *Int. J. Climatol.*, **30**, 418–431, https://doi.org/10.1002/JOC.1893.

Emanuel, K. A., 1986: Overview and definition of mesoscale meteorology. *Mesoscale Meteorology and Forecasting*, P. S. Ray, Ed., Amer. Meteor. Soc., 1–17.

Fairman, J. G., D. M. Schultz, D. J. Kirshbaum, S. L. Gray, and A. I. Barrett, 2016: Climatology of banded precipitation over the contiguous United States. *Mon. Wea. Rev.*, **144**, 4553–4568, https://doi.org/10.1175/MWR-D-16-0015.1.

Feng, Z., L. R. Leung, S. Hagos, R. A. Houze, C. D. Burleyson, and K. Balaguru, 2016: More frequent intense and long-lived storms dominate the springtime trend in central US rainfall. *Nat. Commun.*, **7**, 13429, https://doi.org/10.1038/ncomms13429.

——, R. A. Houze, L. R. Leung, F. Song, J. C. Hardin, J. Wang, W. I. Gustafson Jr., and C.R. Homeyer, 2019: Spatiotemporal characteristics and large-scale environments of mesoscale convective systems east of the rocky mountains. *J. Climate*, **32**, 7303–7328, https://doi.org/10.1175/JCLI-D-19-0137.1.

Fiolleau, T., and R. Roca, 2013: An algorithm for the detection and tracking of tropical mesoscale convective systems using infrared images from geostationary satellite. *IEEE Trans. Geosci. Remote Sens.*, **51**, 4302–4315, https://doi.org/10.1109/TGRS.2012.2227762.

Fritsch, J., J. Murphy, and J. Kain, 1994: Warm core vortex amplification over land. *J. Atmos. Sci.*, **51**, 1780–1807, https://doi.org/10.1175/1520-0469(1994)051<1780:WCVAOL>2.0.CO;2.

Geerts, B., and Coauthors, 2017: The 2015 Plains Elevated Convection At Night field project. *Bull. Amer. Meteor. Soc.*, **98**, 767–786, https://doi.org/10.1175/BAMS-D-15-00257.1.

Haberlie, A. M., and W. S. Ashley, 2018: A method for identifying midlatitude mesoscale convective systems in radar mosaics. Part I: Segmentation and classification. *J. Appl. Meteor. Climatol.*, **57**, 1575–1598, https://doi.org/10.1175/JAMC-D-17-0293.1.

——, and ——, 2019: A radar-based climatology of mesoscale convective systems in the United States. *J. Climate*, **32**, 1591–1606, https://doi.org/10.1175/JCLI-D-18-0559.1.

Haghi, K. R., and Coauthors, 2019: Bore-ing into nocturnal convection. *Bull. Amer. Meteor. Soc.*, **100**, 1103–1121, https://doi.org/10.1175/BAMS-D-17-0250.1.

——, D. B. Parsons, and A. Shapiro, 2017: Bores observed during IHOP_2002: The relationship of bores to the nocturnal environment. *Mon. Wea. Rev.*, **145**, 3929–3946, https://doi.org/10.1175/MWR-D-16-0415.1.

Hennon, C. C., C. N. Helms, K. R. Knapp, and A. R. Bowen, 2011: An objective algorithm for detecting and tracking tropical cloud clusters: Implications for tropical cyclogenesis prediction. *J. Atmos. Oceanic Technol.*, **28**, 1007–1018, https://doi.org/10.1175/2010JTECHA1522.1.

Higgins, R., Y. Yao, and X. Wang, 1997: Influence of the North American monsoon system on the U.S. summer precipitation regime. *J. Climate*, **10**, 2600–2622, https://doi.org/10.1175/1520-0442(1997)010<2600:IOTNAM>2.0.CO;2.

Holton, J. R., 1967: The diurnal boundary layer wind oscillation above sloping terrain. *Tellus*, **19**, 200–205, https://doi.org/10.3402/tellusa.v19i2.9766.

Houze, R. A., Jr., 1982: Cloud clusters and large-scale vertical motions in the tropics. *J. Meteor. Soc. Japan*, **60**, 396–410, https://doi.org/10.2151/jmsj1965.60.1_396.

——, 1993: *Cloud Dynamics*. Academic Press, 573 pp.

——, 1997: Stratiform precipitation in regions of convection: A meteorological paradox? *Bull. Amer. Meteor. Soc.*, **78**, 2179–2196, https://doi.org/10.1175/1520-0477(1997)078<2179:SPIROC>2.0.CO;2.

——, 2018: 100 years of research on mesoscale convective systems. *A Century of Progress in Atmospheric and Related Sciences: Celebrating the American Meteorological Society Centennial*, Meteor. Monogr., No. 59, Amer. Meteor. Soc., https://doi.org/10.1175/AMSMONOGRAPHS-D-18-0001.1.

Jirak, I. L., W. R. Cotton, and R. L. McAnelly, 2003: Satellite and radar survey of mesoscale convective system development. *Mon. Wea. Rev.*, **131**, 2428–2449, https://doi.org/10.1175/1520-0493(2003)131<2428:SARSOM>2.0.CO;2.

Johnston, E. C., 1981: Meso-scale vorticity centers induced by mesoscale convective complexes. M.S. thesis, Dept. of Meteorology, University of Wisconsin–Madison, 54 pp.

Laing, A. G., and J. M. Fritsch, 1997: The global population of mesoscale convective complexes. *Quart. J. Roy. Meteor. Soc.*, **123**, 389–405, https://doi.org/10.1002/qj.49712353807.

——, and ——, 2000: The large-scale environments of the global populations of mesoscale convective complexes. *Mon. Wea. Rev.*, **128**, 2756–2776, https://doi.org/10.1175/1520-0493(2000)128<2756:TLSEOT>2.0.CO;2.

Leary, C. A., and R. A. Houze, 1979: Melting and evaporation of hydrometeors in precipitation from the anvil clouds of deep tropical convection. *J. Atmos. Sci.*, **36**, 669–679, https://doi.org/10.1175/1520-0469(1979)036<0669:MAEOHI>2.0.CO;2.

Li, Y., and R. B. Smith, 2010: The detection and significance of diurnal pressure and potential vorticity anomalies east of the Rockies. *J. Atmos. Sci.*, **67**, 2734–2751, https://doi.org/10.1175/2010JAS3423.1.

Li, L., W. Li, and Y. Kushnir, 2012: Variation of the North Atlantic subtropical high western ridge and its implication to southeastern U.S. summer precipitation. *Climate Dyn.*, **39**, 1401–1412, https://doi.org/10.1007/s00382-011-1214-y.

Machado, L., W. Rossow, R. Guedes, and A. Walker, 1998: Life cycle variations of mesoscale convective systems over the Americas. *Mon. Wea. Rev.*, **126**, 1630–1654, https://doi.org/10.1175/1520-0493(1998)126<1630:LCVOMC>2.0.CO;2.

Maddox, R. A., 1980: Meoscale convective complexes. *Bull. Amer. Meteor. Soc.*, **61**, 1374–1387, https://doi.org/10.1175/1520-0477(1980)061<1374:MCC>2.0.CO;2.

——, 1983: Large-scale meteorological conditions associated with midlatitude, mesoscale convective complexes. *Mon. Wea. Rev.*, **111**, 1475–1493, https://doi.org/10.1175/1520-0493(1983)111<1475:LSMCAW>2.0.CO;2.

Mapes, B. E., and R. A. Houze, 1993: Cloud clusters and superclusters over the oceanic warm pool. *Mon. Wea. Rev.*, **121**, 1398–1416, https://doi.org/10.1175/1520-0493(1993)121<1398:CCASOT>2.0.CO;2.

Parker, M. D., and R. H. Johnson, 2000: Organizational modes of midlatitude mesoscale convective systems. *Mon. Wea. Rev.*, **128**, 3413–3436, https://doi.org/10.1175/1520-0493(2001)129<3413:OMOMMC>2.0.CO;2.

Parsons, D. B., K. R. Haghi, K. T. Halbert, B. Elmer, and J. Wang, 2019: The potential role of atmospheric bores and gravity waves in the initiation and maintenance of nocturnal convection over the southern Great Plains. *J. Atmos. Sci.*, **76**, 43–68, https://doi.org/10.1175/JAS-D-17-0172.1.

Peters, J. M., and R. S. Schumacher, 2014: Objective categorization of heavy-rain-producing MCS synoptic types by rotated principal component analysis. *Mon. Wea. Rev.*, **142**, 1716–1737, https://doi.org/10.1175/MWR-D-13-00295.1.

Prein, A. F., C. Liu, K. Ikeda, R. Bullock, R. M. Rasmussen, G. J. Holland, and M. Clark, 2017: Simulating North American mesoscale convective systems with a convection-permitting climate model. *Climate Dyn.*, https://doi.org/10.1007/s00382-017-3993-2, in press.

Raymond, D., and H. Jiang, 1990: A theory for long-lived mesoscale convective systems. *J. Atmos. Sci.*, **47**, 3067–3077, https://doi.org/10.1175/1520-0469(1990)047<3067:ATFLLM>2.0.CO;2.

Reif, D. W., and H. B. Bluestein, 2017: A 20-year climatology of nocturnal convection initiation over the central and southern Great Plains during the warm season. *Mon. Wea. Rev.*, **145**, 1615–1639, https://doi.org/10.1175/MWR-D-16-0340.1.

Riley, G. T., M. G. Landin, and L. F. Bosart, 1987: The diurnal variability of precipitation across the central Rockies and adjacent Great Plains. *Mon. Wea. Rev.*, **115**, 1161–1172, https://doi.org/10.1175/1520-0493(1987)115<1161:TDVOPA>2.0.CO;2.

Song, F., Z. Feng, L. R. Leung, R. A. Houze, J. Wang, J. Hardin, and C. R. Homeyer, 2019: Contrasting spring and summer large-scale environments associated with mesoscale convective systems over the U.S. Great Plains. *J. Climate*, **32**, 6749–6767, https://doi.org/10.1175/JCLI-D-18-0839.1.

Stensrud, D. J., 1996: Importance of low-level jets to climate: A review. *J. Climate*, **9**, 1698–1711, https://doi.org/10.1175/1520-0442(1996)009<1698:IOLLJT>2.0.CO;2.

Thompson, R. L., B. T. Smith, J. S. Grams, A. R. Dean, and C. Broyles, 2012: Convective modes for significant severe thunderstorms in the contiguous United States. Part II: Supercell and qlcs tornado environments. *Wea. Forecasting*, **27**, 1136–1154, https://doi.org/10.1175/WAF-D-11-00116.1.

Tian, B., I. M. Held, N.-C. Lau, and B. J. Soden, 2005: Diurnal cycle of summertime deep convection over North America: A satellite perspective. *J. Geophys. Res.*, **110**, D08108, https://doi.org/10.1029/2004JD005275.

Trier, S. B., and D. B. Parsons, 1993: Evolution of environmental conditions preceding the development of a nocturnal mesoscale convective complex. *Mon. Wea. Rev.*, **121**, 1078–1098, https://doi.org/10.1175/1520-0493(1993)121<1078:EOECPT>2.0.CO;2.

Vila, D. A., L. A. T. Machado, H. Laurent, and I. Velasco, 2008: Forecast and tracking the evolution of cloud clusters (FORTRACC) using satellite infrared imagery: Methodology and validation. *Wea. Forecasting*, **23**, 233–245, https://doi.org/10.1175/2007WAF2006121.1.

Wang, S.-Y., and T.-C. Chen, 2009: The late-spring maximum of rainfall over the U.S. central plains and the role of the low-level jet. *J. Climate*, **22**, 4696–4709, https://doi.org/10.1175/2009JCLI2719.1.

Weaver, S. J., and S. Nigam, 2008: Variability of the Great Plains low-level jet: Large-scale circulation context and hydroclimate impacts. *J. Climate*, **21**, 1532–1551, https://doi.org/10.1175/2007JCLI1586.1.

——, S. Schubert, and H. Wang, 2009: Warm season variations in the low-level circulation and precipitation over the central United States in observations, AMIP simulations, and idealized SST experiments. *J. Climate*, **22**, 5401–5420, https://doi.org/10.1175/2009JCLI2984.1.

Weckwerth, T. M., and U. Romatschke, 2019: Where, when, and why did it rain during PECAN? *Mon. Wea. Rev.*, **147**, 3557–3573, https://doi.org/10.1175/MWR-D-18-0458.1.

——, J. Hanesiak, J. W. Wilson, S. B. Trier, S. K. Degelia, W. A. Gallus Jr., R. D. Roberts, and X. Wang, 2019: Nocturnal convection initiation during PECAN 2015. *Bull. Amer. Meteor. Soc.*, **100**, 2223–2239, https://doi.org/10.1175/BAMS-D-18-0299.1.

Whitehall, K., and Coauthors, 2015: Exploring a graph theory based algorithm for automated identification and characterization of large mesoscale convective systems in satellite datasets. *Earth Sci. Inform.*, **8**, 663–675, https://doi.org/10.1007/s12145-014-0181-3.

Williams, M., and R. A. Houze, 1987: Satellite-observed characteristics of winter monsoon cloud clusters. *Mon. Wea. Rev.*, **115**, 505–519, https://doi.org/10.1175/1520-0493(1987)115<0505:SOCOWM>2.0.CO;2.

Wolyn, P. G., and T. B. Mckee, 1994: The mountain-plains circulation east of a 2-km-high north–south barrier. *Mon. Wea. Rev.*, **122**, 1490–1508, https://doi.org/10.1175/1520-0493(1994)122<1490:TMPCEO>2.0.CO;2.

Yang, Q., R. A. Houze, L. R. Leung, and Z. Feng, 2017: Environments of long-lived mesoscale convective systems over the central United States in convection permitting climate simulations. *J. Geophys. Res. Atmos.*, **122**, 13 288–13 307, https://doi.org/10.1002/2017JD027033.

Yuter, S. E., and R. A. Houze, 1995: Three-dimensional kinematic and microphysical evolution of Florida cumulonimbus. Part III: Vertical mass transport, mass divergence, and synthesis. *Mon. Wea. Rev.*, **123**, 1964–1983, https://doi.org/10.1175/1520-0493(1995)123<1964:TDKAME>2.0.CO;2.